

pubs.acs.org/JPCC Article

# Thermal Stability of Semiconductor Nanocrystal Solids: Understanding Nanocrystal Sintering and Grain Growth

Published as part of The Journal of Physical Chemistry virtual special issue "Horst Weller Festschrift". Wenyong Liu, Vishwas Srivastava, J. Matthew Kurley, Chengyang Jiang, and Dmitri V. Talapin\*



Cite This: J. Phys. Chem. C 2022, 126, 21136-21148



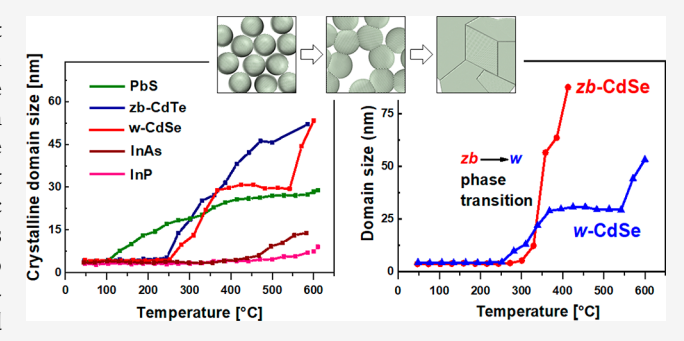
**ACCESS** I

III Metrics & More

Article Recommendations

SI Supporting Information

ABSTRACT: Nanomaterials are naturally metastable with respect to bulk solids. This raises the very important fundamental problem of their morphological stability, especially when nanoscale crystallites are touching or nearly touching each other, such as in thin-film devices. In some cases, nanostructuring must be preserved under operational conditions (e.g., in quantum dot LEDs, lasers, photodetectors, and nanogranular thermoelectric devices). In other cases, we use nanocrystalline particles as precursors to a material with large crystalline grains and aim to sinter them as efficiently as possible (e.g., in polycrystalline thin-film solar cells). We carried out a systematic study of sintering and grain growth in materials composed of various sub-10 nm



semiconductor grains. The boundaries between individual semiconductor grains have been chemically engineered using inorganic surface ligands. We found that the early stages of sintering and grain growth of nanocrystalline semiconductors are controlled by the ion mobility at the nanocrystal surfaces, while the late stages of grain growth are controlled by the mobility of the grain boundaries. This appears to be a general phenomenon for semiconductor nanocrystals, and it leads to several interesting and counterintuitive trends. For example, III–V InAs nanocrystals are generally much more resilient against sintering and grain growth compared to II–VI CdSe nanocrystals even though bulk CdSe has significantly higher melting point temperature than InAs (1268 °C vs 942 °C). Grain growth can be dramatically accelerated when coupled to solid–solid phase transitions. These findings expand our toolbox for rational design of nanocrystal materials for different applications.

# 1. INTRODUCTION

Solution-processed colloidal nanocrystal (NC) inks have emerged as cost-efficient building blocks for the fabrication of optoelectronic devices such as light-emitting diodes (LEDs), photodetectors, solar cells, thermoelectric elements, and printable electronic circuits. The performance of these devices is dependent on the properties of NCs used in device active layers. The size, shape, composition, and connectivity of semiconductor NCs define their properties, such as bandgap energy, emission color, recombination rate, thermal conductivity, and charge carrier mobility. 1-5 Even though the behaviors of individual NCs and their ensembles in solution are well-studied, little work has been dedicated to the evolution of NC layers at elevated temperatures and the understanding of their thermal stability, which are crucial for device fabrication and operation. To elucidate this, two contrasting examples can be given. When using quantum confinement to tune the spectral response of quantum dot light-emitting devices or lasers, it is important that NCs perfectly maintain their stability against sintering and grain growth induced by elevated temperatures during device fabrication and operation.<sup>5-8</sup> In other cases, e.g., for solar cells made of CdTe,

CuIn<sub>x</sub>Ga<sub>1-x</sub>Se<sub>2</sub> (CIGS), or Cu<sub>2</sub>ZnSnS<sub>4</sub> (CZTS) NCs, fast and efficient sintering and recrystallization of sub-10 nm NCs into micron-sized crystalline grains are desired to create an absorber layer with low concentration of recombination sites at the grain boundaries.<sup>9–11</sup> The above examples illustrate the importance of NC sintering and grain growth behavior, but surprisingly little attention has been paid to understanding the thermal stability of films prepared from colloidal NCs.

Thermal treatment of NC films causes the NCs to fuse and ripen, which is accompanied by an increase in the average NC size. The concepts of sintering and grain growth have been originally developed by the ceramics community, where sintering was related to densification and the microstructure changes occurring during densification (neck formation, grain

Received: October 21, 2022 Revised: November 3, 2022 Published: December 5, 2022





boundary formation, pore size decrease, etc.).<sup>12</sup> One has to be careful with nomenclature because the nanomaterials community often has used the term sintering to describe the transformation of discrete NC assemblies into a material composed of connected, fused, or ripened crystalline domains, without emphasis on densification. This implicitly treats grain growth as a part of sintering rather than as a separate process. <sup>13,14</sup>

Sintering of micron and submicron powders is routinely used to improve mechanical properties, to increase electrical and thermal conductivity in ceramics, in powder metallurgy, for fabricating thermoelectric materials, and so on.  $^{15-17}$  On the other hand, preventing sintering of catalytically active metal clusters is an active area of research in heterogeneous catalysis. Real Colloidally synthesized NCs bridge the size gap between micron-sized ceramic powders and metal clusters, which are typically smaller than 2 nm. Sintering and grain growth of ALD-passivated PbS NCs, superlattices of PbSe NCs, CIGS NCs, and CZTS nanorods have been studied; 13,14,23-25 however, a systematic understanding of NC sintering and grain growth is largely lacking. Sintering studies of as-synthesized colloidal NCs are complicated by organic surface ligands that separate inorganic NC cores at room temperature but desorb and decompose upon heating.<sup>23</sup> With organic ligands, the sintering and grain growth processes are strongly dependent on sample history, which makes systematic studies and data interpretation difficult. In recent years, our group and others have developed methods to replace the longchain organic ligands with a variety of compact inorganic ligands such as chalcogenidometallates, chalcogenides, halides, and halometallates. 6,7,26 The inorganic ligands facilitate charge transport through NC films, improving the characteristics of optoelectronic devices. 6,7,27,28 The inorganic ligands also have clean and well-defined reactivity at elevated temperatures, 29,30 in contrast to complex carbonization chemistry of organic ligands.31

In this work, we investigate the effects of NC size, surface, and phase on the sintering and grain growth behavior of all-inorganic semiconductor NC films. We also investigate general trends for NCs belonging to II–VI, III–V, and IV–VI semiconductor families and provide a generalized description of the sintering and grain growth process in NC solids at temperatures relevant to thin-film processing of NC devices.

# 2. METHODS

**2.1.** Nanocrystal Synthesis. Zinc blende (zb-) and wurtzite (w-) phase CdSe NCs, zb- and w-CdTe, zb-InP, zb-InAs, rock salt PbS, kesterite (k-), and wurtzite (w-) Cu<sub>2</sub>ZnSnS<sub>4</sub> (CZTS) were all synthesized following reported protocols. zb-CdSe NCs were prepared with SeO2 and cadmium myristate at 240 °C, following Cao et al.<sup>32</sup> w-CdSe NCs were obtained with Se:TOP and CdO as precursors and ODPA as the surfactant at 370 °C following Manna et al. 33 zband w-CdTe NCs were synthesized with octadecylphosphonic acid (ODPA) and oleic acid (OA) as the surfactants, respectively, following Peng et al.<sup>34</sup> Trioctylphosphine (TOP) and trioctylphosphine oxide (TOPO) capped InP were synthesized at 270 °C overnight using Micic's recipe. 35 4 nm TOP-capped InAs NCs were obtained with two additional injections with InCl<sub>3</sub> and (TMS)<sub>3</sub>As as the precursors using Guzelian's recipe.<sup>36</sup> PbS NCs were synthesized using the protocol by Hines et al.<sup>37</sup> k-CZTS was synthesized using the recipe of Riha et al., 38 and w-CZTS was synthesized using the

protocol by Jao et al.<sup>39</sup> Necessary modifications were performed to obtain the desired size and morphology.

2.2. Preparation of  $(N_2H_5)_2In_2Se_4$  and  $(NH_4)_2S$ -Capped zb- and w-CdSe, (N2H5)2In2Se4-Capped InAs and InP NCs, (N2H5)2In2Te4-Capped CdTe NCs, and (NH<sub>4</sub>)<sub>2</sub>S-Capped w- and k-CZTS Inks. A two-phase ligand exchange approach was performed with toluene and  $N_2H_4$  as the top and bottom phases, respectively. Ligand exchange duration ranges from 30 min to 3 h, depending on the ligands used during synthesis. ODPA-capped w-CdSe normally takes a few hours before the ligand exchange completes, whereas TOP-capped InAs NCs finish the ligand exchange with  $(N_2H_5)_2In_2Se_4$  within 30 min.  $N_2H_4$  is used as the polar solvent, based on the following arguments: first, it is a good solvent to disperse most inorganic ligand-capped NCs; second, it is a volatile solvent which can be removed after annealing at 80 °C for 30 min on the hot plate; and third, even the residue which remains adsorbed to the surface can cleanly decompose into N<sub>2</sub> and H<sub>2</sub> at elevated temperature.

 $({\rm NH_4})_2{\rm S}$  can only exist in aqueous solution. Since moisture is found to greatly suppress NC sintering, an amount of  $({\rm NH_4})_2{\rm S}$  just sufficient to complete phase transfer was used for the ligand exchange. For example, for 0.2 mL CdSe NCs (60 mg/mL), 5  $\mu{\rm L}$   $({\rm NH_4})_2{\rm S}$  aqueous solution (48% by weight) was used. The inorganic ligand-capped NCs were meticulously washed to remove any remaining free ligands. The as-prepared N<sub>2</sub>H<sub>4</sub> solution of inorganic ligand-capped NCs was passed through a 0.2  $\mu{\rm m}$  PTFE filter before being precipitated with such an amount of acetonitrile that a slight nanocrystal color was left in the supernatant. The precipitate was redispersed into N<sub>2</sub>H<sub>4</sub>, and filtration was performed again. In a similar way, a second precipitation cycle was performed to completely separate free ligands from nanocrystals.

**2.3. Preparation of "Bare" zb- and w-CdSe NC Inks.** Both ODPA and carboxylic acid on the surfaces of w- and zb-CdSe NCs were stripped with HBF<sub>4</sub> solution or Me<sub>3</sub>OBF<sub>4</sub> powder in hexane. The NC precipitate was then dissolved into DMF for purification, which is an important step to remove impurities. The NC solution in DMF was filtered through a 0.2  $\mu$ m PTFE filter and precipitated with toluene. The precipitate was then mixed with N<sub>2</sub>H<sub>4</sub> to form suspensions for the XRD sample preparation.

- **2.4. Preparation of NC Films.** Highly concentrated solutions with concentrations up to 40–60 mg/mL were drop-cast onto oxygen-plasma-treated silicon wafers with a 300 nm silicon dioxide surface layer. The NC film was annealed at 100 °C on the hot plate inside a glovebox for 30 min to remove the volatile solvent, before it was transferred either into the furnace for higher-temperature annealing or to the XRD equipment for the in situ measurements.
- **2.5. Preparation of (NH<sub>4</sub>)<sub>2</sub>S-Capped PbS NC Film.** Sulfide-capped PbS NCs were obtained by treating a PbS NC film with  $(NH_4)_2S$  solution, following literature procedures.<sup>40</sup>
- **2.6.** In Situ and Ex Situ XRD Measurements. Diffraction patterns were obtained with a Bruker D8 diffractometer with a Cu  $K\alpha$  X-ray source, operating at 40 kV and 40 mA, and a Vantec 2000 area detector. Two kinds of sintering experiments were performed: ex situ and in situ XRD measurements. For ex situ sintering, the NC film was annealed in a furnace inside the glovebox from low to high temperature, and corresponding P-XRD patterns were collected after each annealing period. In detail, the NC film was transferred into the furnace, which was preset to a certain temperature, and annealed for 10 min before

being taken out for P-XRD measurement. The temperature was monotonically increased from 50 to 600 °C in steps of 25 or 50 °C. During the whole process, the same NC film was used. To minimize temperature fluctuations and annealing duration variances when comparing the thermal stability of different samples, those samples' annealing steps were performed at the same time in the same furnace.

For in situ XRD experiments, on the other hand, the sample was loaded onto a holder covered by an airtight dome in the XRD equipment chamber. An air-free environment was achieved by evacuation and refilling of the chamber with  $\rm N_2$  three times. An amount of 1 atm of  $\rm N_2$  was used to protect the sample from oxidation during elevated temperature XRD measurement. The sample was heated from room temperature to 600 °C, with a ramp rate of 3 °C/min. Meanwhile, continuous XRD measurements were performed, with each pattern acquisition taking 9 min. In total, around 21 XRD patterns were collected during each run, with each covering an approximately 27 °C range.

**2.7. SEM Studies.** SEM images were acquired with an FEI Nova NanoSEM 200 operated at 10.0 kV. The SEM samples were prepared by drop-casting an NC solution onto silicon wafers, followed by annealing in the furnace inside the glovebox with the same temperature ramp rate as in the XRD measurements. In order to observe the morphologies of the top, bottom, and cross-sectional regions of the films, they were scratched into powders with razor blades and then rinsed with one drop of acetone to improve the attachment of the powder onto the wafer.

2.8. In Situ and Ex Situ TEM Studies. For ex-situ TEM, the images were taken by using an FEI Tecnai F30 microscope operating at 300 kV. In situ and ex situ TEM samples were prepared by drop-casting dilute NC solutions in N<sub>2</sub>H<sub>4</sub> onto Au and Cu grids, respectively. These were then annealed at 80 °C for 30 min on the hot plate to remove volatile solvent. For in situ TEM, the sample was directly loaded onto a TEM sample holder with a heating setup. As a tentative measure to prevent the sublimation of NCs at elevated temperature, another Au grid was used to cover the TEM sample in one case. Heating power was manually controlled to maintain a similar temperature ramp rate to that of the XRD and SEM runs. A series of TEM images were taken while the temperature was ramping up. For ex situ TEM, as-prepared samples were transferred into the furnace for further annealing at various temperatures. The annealing in the furnace followed the same schedule as in the ex situ XRD and SEM measurements.

**2.9. Solution and Thin-Film Absorption Spectra Measurements.** A Cary 5000 UV—vis spectrophotometer was used for both solution and thin-film absorption measurements. A DRA 2500 diffuse reflectance accessory (integrating sphere) was used to record both transmittance and reflectance for the thin-film absorption. For thin-film absorption spectra, film quality and thickness directly determine the signal-to-noise ratio of the spectrum. Therefore, the film was prepared on a 2"  $\times$  2" quartz plate by spin-coating with a concentrated solution (40–60 mg/mL). The film was annealed according to the schedules above in the furnace inside the glovebox before the absorption spectrum measurements.

## 3. RESULTS AND DISCUSSION

**3.1. Preparation of Nanocrystal Films for Sintering and Grain Growth Experiments.** Colloidal CdSe, CdTe, PbS, InP, InAs, and CZTS NCs were synthesized according to

the established protocols with slight modifications as needed to obtain a desired size and morphology. CdSe and CdTe NCs have been synthesized in two polymorphs, hexagonal wurtzite (w) and cubic zinc blende (zb). Wurtzite and kesterite (k) polymorphs have been synthesized for CZTS NCs. The original long-chain hydrocarbon surfactants were replaced with inorganic ligands such as  $(N_2H_5)_2In_2Se_4$ ,  $(N_2H_5)_2In_2Te_4$ , and (NH<sub>4</sub>)<sub>2</sub>S using a two-phase ligand exchange approach. <sup>26,41</sup> To minimize the introduction of heterogeneous atoms, we paired the inorganic ligand and NCs in such a way that either the cation or anion in both the NC and the ligand was identical. As an example,  $(N_2H_5)_2In_2Se_4$  was used as the capping ligand for CdSe, InAs, and InP NCs;  $(N_2H_5)_2In_2Te_4$  was used to passivate CdTe NCs; and (NH<sub>4</sub>)<sub>2</sub>S was used for PbS and CZTS NCs. Ligand-free NCs were prepared by treating NCs with ligand-stripping agents such as HBF<sub>4</sub> and Me<sub>3</sub>OBF<sub>4</sub>. 41,42 We used the minimal amount of inorganic surface ligands sufficient to provide colloidal stability. To eliminate the solvent effects, we used N<sub>2</sub>H<sub>4</sub> as solvent for colloidal NCs. (Note: hydrazine is a hazardous solvent which is explosive when reacting with oxygen at elevated temperature. Appropriate precautions should be exercised while handling hydrazine.) Unlike many highboiling polar solvents which tend to decompose, forming nonvolatile residues, hydrazine has a low boiling point, and its thermal decomposition products are N2, NH3, and H2 which immediately escape from the film. The absorption spectra after surface modification indicate that the NCs retained their size and size distribution (Figure S1). The NC inks were then spincoated onto Si substrates and dried at 100 °C for 1 h. (NH<sub>4</sub>)<sub>2</sub>S-capped PbS NC films were obtained by an on-film ligand exchange process where a film of PbS NCs capped with oleate ligands was dipped into (NH<sub>4</sub>)<sub>2</sub>S solution, following a reported protocol.40 This was done to avoid oriented attachment and coarsening during the two-phase ligand exchange process for PbS NCs. 43 For all studied samples, the film thickness was on the order of a micron (Figure S2), and the highest temperature used in this study was 600 °C. No significant material sublimation at ambient pressure was observed at this temperature. As-deposited NC films showed short-range order and could be approximated by randomly packed spheres, which are reported to have up to 64% volume packing density.44,45

By using a combination of powder X-ray diffraction (P-XRD), electron microscopy, and optical absorption measurements, we followed the evolution of structure and morphology of semiconductor NC films subjected to thermal treatments at different temperatures. The early stages of NC sintering and grain growth can be investigated by monitoring the evolution of the optical absorption spectra because NC necking boosts electronic coupling between semiconductor NCs and causes broadening and red shifting in their absorption spectra. On the other hand, P-XRD is a powerful tool to track the later stages of NC grain growth. The analysis of P-XRD patterns provides information about the NC phase and the average size of crystalline domains, as calculated from the Scherrer equation. It is important to add that changes of XRD crystallite size can occur with or without changes in average density and should not be used to assess densification without additional experimental support. Both grain growth and densification are different thermally activated processes, so while density and grain size increases can be simultaneously observed as the annealing temperature is increased, one should not draw a conclusion that the grain size increase caused the density

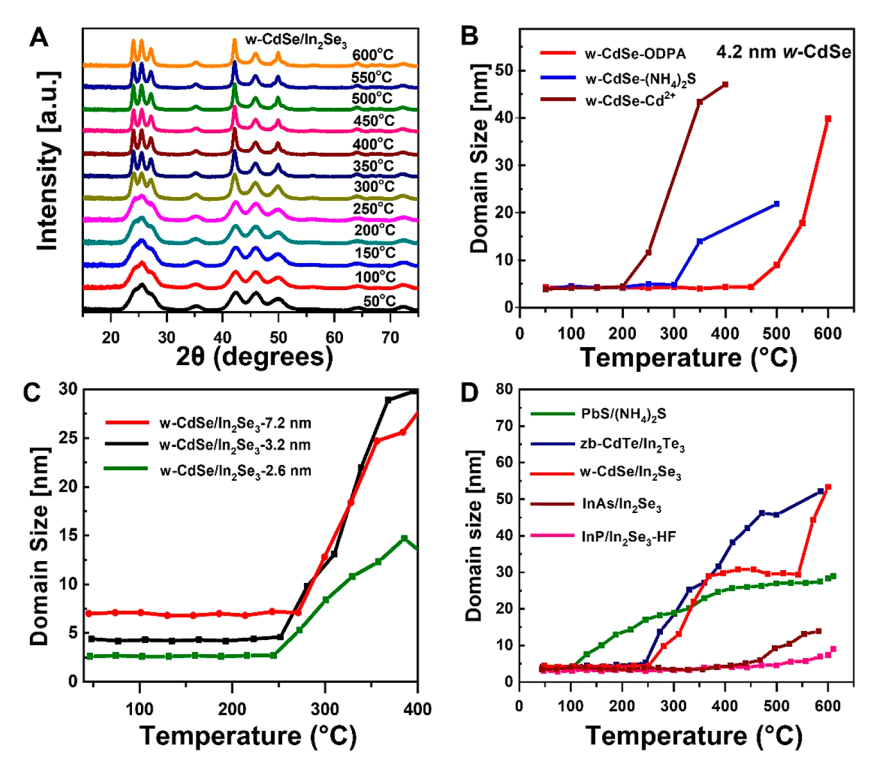


Figure 1. (A) X-ray diffraction patterns of a film of 4 nm w-CdSe NCs capped with  $In_2Se_4^{2-}$  ligands heated to different temperatures in situ. The NC films, named here w-CdSe/ $In_2Se_3$ , were prepared by drop casting a hydrazine solution of w-CdSe NCs capped with  $(N_2H_5)_2In_2Se_4$  ligands. These ligands decomposed to  $In_2Se_3$  upon heating.<sup>48</sup> (B) Grain growth for w-CdSe NCs capped with *n*-octadecylphosphonic acid (ODPA),  $(NH_4)_2S$ , and "bare" CdSe NCs colloidally stabilized with  $BF_4^-$  counterions.<sup>41</sup> (C) Grain growth profiles for films of three differently sized w-CdSe NCs all capped with  $(N_2H_5)_2In_2Se_4$  ligands. (D) Comparison of grain growth profiles for different semiconductor NCs capped with cation-/anion-matched inorganic ligands.

increase or vice versa. SEM and TEM measurements provide additional insights into the morphology, density, and grain size of annealed NC films, including those needed to make this distinction. For ex situ experiments, the NC films were annealed in a furnace preset to a certain temperature for 10 min inside an N2 glovebox. The temperature was steadily increased from 50 to 600 °C, in steps of 25 or 50 °C (Figure S3a). We also carried out in situ P-XRD experiments where the NC film was placed under a nitrogen atmosphere inside an airtight dome (Figure S4). The sample was heated from room temperature to 600 °C with a ramp rate of 3 °C/min. Meanwhile, continuous recording of P-XRD patterns was carried out, with each pattern acquisition taking 9 min. In total, 21 P-XRD patterns were collected during a full temperature ramp, with each pattern covering a range of approximately 27 °C (Figure S3b).

**3.2. Onset of Nanocrystal Sintering and Grain Growth.** We found that NC sintering starts at much lower temperatures compared to sintering and grain growth of bulk powders, similar to the melting point depression effect observed for metal and semiconductor NCs.  $^{46,47}$  For example, 4 nm w-CdSe NCs capped with  $(N_2H_5)_2In_2Se_4$  surface ligands start to sinter between 250 and 300 °C, far below the bulk CdSe melting temperature of 1268 °C. Figure 1a shows a series of X-ray diffraction patterns collected for a film of  $(N_2H_5)_2In_2Se_4$ -capped w-CdSe NCs as it was heated from 50 to 600 °C with a ramp rate of 3 °C/min. With an increase of the annealing temperature, the width of all diffraction peaks decreased due to the increase of the crystalline domain size. The onset of sintering around 250 °C was also evident from the changes of the absorption spectra of w-CdSe NC films

(Figure S5), which show smearing of the first excitonic peak starting at 225 °C as the NCs are joined together due to the decomposition of  $(N_2H_5)_2In_2Se_4$  to  $In_2Se_3$ .<sup>48</sup> Densification of the NC films after heat treatment is evident from SEM images in Figure S2, where the top view of the film after a 450 °C thermal treatment shows extensive cracking. This cracking is due to stress that develops due to constrained sintering (densification): the film shrinks laterally, but the substrate does not; hence, a tensile stress develops that causes cracking.<sup>49</sup>

3.3. Effect of Nanocrystal Surface Ligands on Sintering and Grain Growth. To better understand the role of surfactants in the process of NC sintering and grain growth, we compared the grain growth profiles for 4.2 nm w-CdSe NCs capped with three different types of surface ligands. As-synthesized w-CdSe NCs were capped with *n*-octadecylphosphonic acid (ODPA). The pristine ODPA ligands can be stripped with Cd(BF<sub>4</sub>)<sub>2</sub> to prepare "bare" CdSe NCs where the surface of CdSe NCs is positively charged with an excess of  $Cd^{2+}$  ions. Finally,  $(NH_4)_2S$  and  $(N_2H_5)_2In_2Se_4$  were used as inorganic ligands. Figure 1b shows the grain growth of CdSe NCs with different surface ligands. Bare CdSe NCs with a cadmium-rich surface started grain growth at 200 °C, whereas for  $(NH_4)_2$ S-capped CdSe NCs grain growth began at 300 °C. Grain growth was found to be significantly impeded for ODPA-capped CdSe NCs, where narrowing of the X-ray diffraction peaks was observed only above 450 °C (see Figure S6 for P-XRD patterns). As discussed below, the early stage of NC sintering is defined by the diffusion of ions at the NC surface. 50 The nature of chemical bonding between the capping ligands and surface atoms of the NC core plays an important role in tuning surface energy, which in turn affects

the rate of surface diffusion. In CdSe, cadmium cations are smaller and significantly more mobile than selenide anions. We can speculate that the Cd-rich surface of "bare" CdSe NCs facilitates the rate-limiting step, surface diffusion of Se<sup>2-</sup> ions, during the early phase of grain growth. On the other hand, CdSe NCs with (NH<sub>4</sub>)<sub>2</sub>S surface ligands upon heating undergo ligand decomposition, forming CdSe NCs with sulfideterminated surfaces favorable for surface diffusion of cations but not optimal for rate-limiting anion diffusion. The CdSe NCs with inorganic ligands show an appreciably lower grain growth onset temperature as compared to CdSe NCs capped with bulky ODPA ligands. ODPA molecules have aliphatic hydrocarbon tails about 2.5 nm long<sup>52</sup> that decompose into amorphous carbon above 400 °C. The nonvolatile layer of amorphous carbon effectively inhibits surface diffusion between NCs and encapsulates NC cores inside graphitic shells.5

NCs with compact ligands are expected to demonstrate more efficient sintering due to tighter interparticle contacts (Figure 1b). A small distance between NC cores in a NC film determines the ease of neck formation between NCs, which is a prerequisite for grain growth. In the presence of ODPA and other bulky organic surface ligands, the initial spacing between 4.2 nm w-CdSe NC cores is much larger than the hopping distance of an atom diffusing between neighboring surface sites, which inhibits the NC necking process. S4

Impurity doping of the lattice can also impact sintering and grain growth, as has been observed for ceramic powders. We tried to minimize the influence of impurity dopants in our study by using ligands that share at least one of their ions with the NC lattice. In the case of "bare" w-CdSe NCs with BF<sub>4</sub><sup>-</sup> counterions, the doping of B or F into a NC lattice is unlikely due to very large B–F bond energy. Generally, we did not notice NC–(inorganic ligand) pairs with pronounced doping-induced acceleration or suppression of NC sintering and grain growth.

**3.4. Effect of NC Size.** Since the surface-to-volume ratio in NCs is strongly dependent on the NC size, we compared the grain growth onset temperatures of different sizes of CdSe NCs capped with In<sub>2</sub>Se<sub>4</sub><sup>2</sup> ligands (Figures 1c and S7). The grain growth onset temperatures for smaller particles were slightly lower due to their larger surface to volume ratio. Even though the profiles were qualitatively similar, the final grain sizes at 400 °C were relatively smaller for 2.6 nm particles, likely because the density of grain boundaries was significantly larger in the films made of partially sintered small NCs compared to the films made of larger NCs.

**3.5.** Sintering and Grain Growth Behavior of Different Semiconductor Nanocrystals. We carried out a comparative study of different NCs belonging to II–VI, III–V, and IV–VI semiconductor families. w-CdSe (hexagonal crystal lattice) and zb-CdTe (cubic lattice) are typical II–VI semiconductors corresponding to thermodynamically stable phases of bulk solids. zb-InAs and zb-InP were chosen as typical examples of III–V compounds with cubic zinc blende crystal structure, while PbS with cubic rock salt structure is a typical IV–VI compound. All of these NCs have nearly spherical shapes and sizes of about 4 nm, and their surfaces were capped with ion-sharing chalcogenidometallate inorganic ligands for consistent comparison.

A comparison of grain size evolution trajectories with temperature for various NCs is shown in Figures 1d, S6, and S8. The lowest temperature onset of grain growth was

observed for PbS NCs (~100 °C). Grain growth in the case of II–VI CdSe and CdTe NCs started at around 250 °C, while III–V InAs and InP NCs showed the highest resilience to heat-induced structural transformations, having no appreciable grain growth below ~450 °C. Strikingly, there is no correlation between the grain growth onset and melting point temperatures of the corresponding bulk phases: InAs ( $T_{\rm m}$  = 942 °C) < InP (1062 °C) < CdTe (1092 °C) < PbS (1114 °C) < CdSe (1258 °C).

A comparison of X-ray diffraction patterns of zb-InAs and w-CdSe NCs at different temperatures, presented as 2D maps (Figure 2), highlights a drastic difference in the thermal

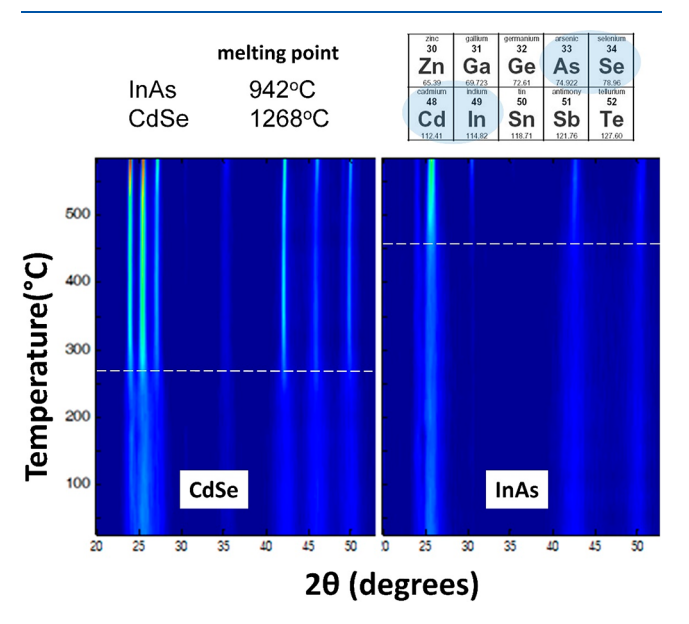


**Figure 2.** Two-dimensional representations of X-ray diffraction patterns measured in situ at different temperatures for 4 nm zb-InAs and 4 nm w-CdSe NCs capped with  $(N_2H_5)_2\text{In}_2\text{Se}_4$  ligands. The dotted lines indicate the temperatures corresponding to the onset of grain growth.

stability of typical II-VI and III-V compounds sharing tetrahedral coordination and very similar lattice parameters. InAs NCs remain intact up to temperatures above 400 °C, whereas the X-ray reflections of w-CdSe NCs start sharpening at temperatures below 300  $^{\circ}\text{C}$ . The difference in thermal stability for II-VI and III-V NCs is also evident from the absorption spectra of annealed NC films (Figure S9). For InAs NC films, the size-dependent excitonic transitions can be clearly observed in films annealed at 300 °C. On the other hand, the absorption peak related to the first excitonic transition in CdSe NCs continuously red shifts upon heating and is completely smeared out at 300 °C, indicating significant necking and ripening in these NCs. It is important to emphasize that the melting point of bulk CdSe (1258 °C) is over 300 °C higher than that of InAs (942 °C), which strongly suggests that NC sintering and grain growth behavior cannot be directly correlated with the melting points of their bulk counterparts.

**3.6. Kinetics of NC Grain Growth.** Our experimental data suggest that, for the films of semiconductor NCs, grain growth kinetics can show rather complex and counterintuitive behavior. Figure 3a shows isothermal grain growth in films of 4 nm w-CdSe NCs capped with  $(N_2H_5)_2In_2Se_4$  surface ligands. At 250 °C a very slow but steady increase of the grain

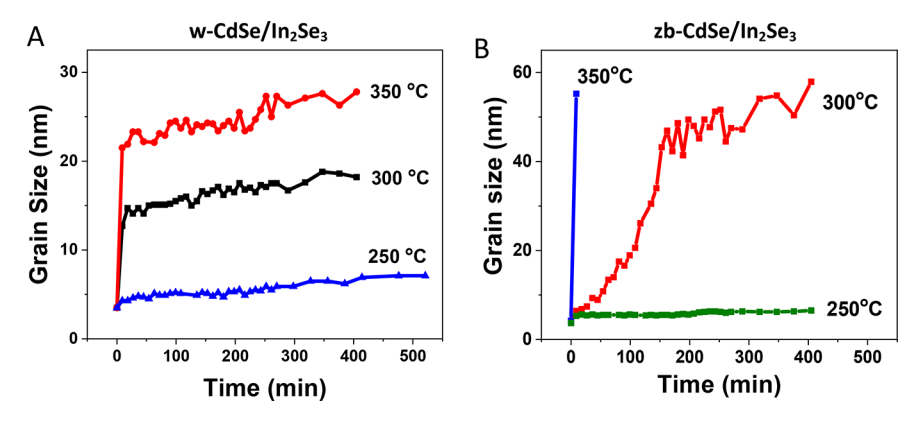
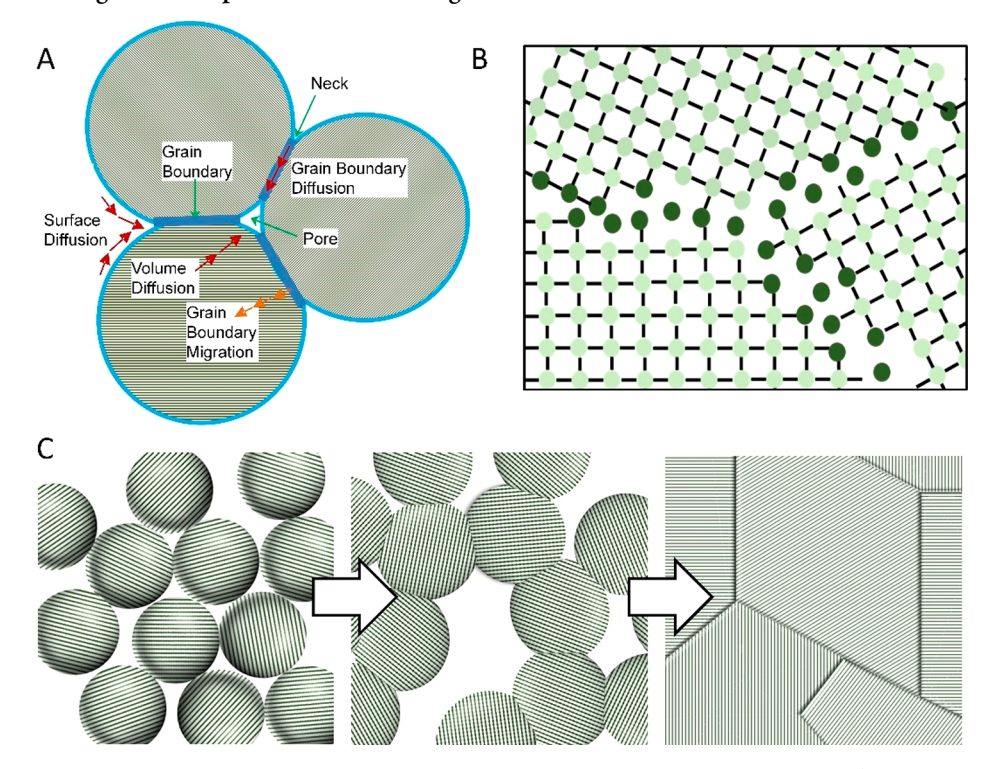


Figure 3. (A) Time evolution of crystalline domain size for a film of wurtzite CdSe NCs with  $(N_2H_5)_2In_2Se_4$  surface ligands held at different temperatures. (B) Time-dependent evolution of crystal size for zinc blende CdSe NCs of similar original size and with the same surface ligands.

Scheme 1. Phenomenological Description of NC Sintering and Grain Growth Processes



<sup>a</sup>(A) Upon heating, individual NCs touch and form necks and grain boundaries. Different diffusion channels (surface, grain boundary, volume) determine the dynamics of NC sintering and grain growth. (B) Schematic representation of vacancies and defects at grain boundaries. (C) Sintering and grain growth in films of semiconductor NCs. From left to right: as-deposited NCs separated from each other form necks via surface diffusion upon heating. Further neck growth happens through grain boundary diffusion. Grain growth then takes place via grain boundary migration.

size was observed, with Scherrer size of crystalline domains approaching 7.1 nm after 8.5 h of continuous heating. On the other hand, at 300 and 350 °C we observed two different time scales—a fast grain growth at early times abruptly switching to a regime of slow continuous growth. Likely, there exist two different rate-limiting diffusion mechanisms, corresponding to fast surface diffusion and much slower grain boundary diffusion, as discussed below.

Even more striking behavior was observed for the film of 4 nm zb-CdSe NCs capped with the same  $(N_2H_5)_2In_2Se_4$  surface ligands (Figure 3b). At 250 °C, the grain growth behavior of zb-CdSe NCs was similar to that for w-CdSe NCs, and their Scherrer grain size approached 6.5 nm after 6.5 h of continuous heating. However, heating at 300 °C resulted in

a qualitatively different behavior, with rapid grain growth to  $\sim$ 45 nm during the first 150 min. At 350 °C, the crystalline domains grew from 4 nm to  $\sim$ 55 nm in less than 10 min, approaching the instrumental limit for measuring Scherrer size for this sample. The rate of grain growth changed by almost 3 orders of magnitude over this relatively narrow temperature range. From a practical point of view, such behavior suggests that caution is required when performing and analyzing accelerated stability tests for NC-based devices.

The above examples show that sintering and grain growth of semiconductor NCs are rather complex phenomena. A better understanding is critical for evaluating the thermal stability of semiconductor nanostructures and the rational development of thermally robust NC layers for optoelectronic devices.

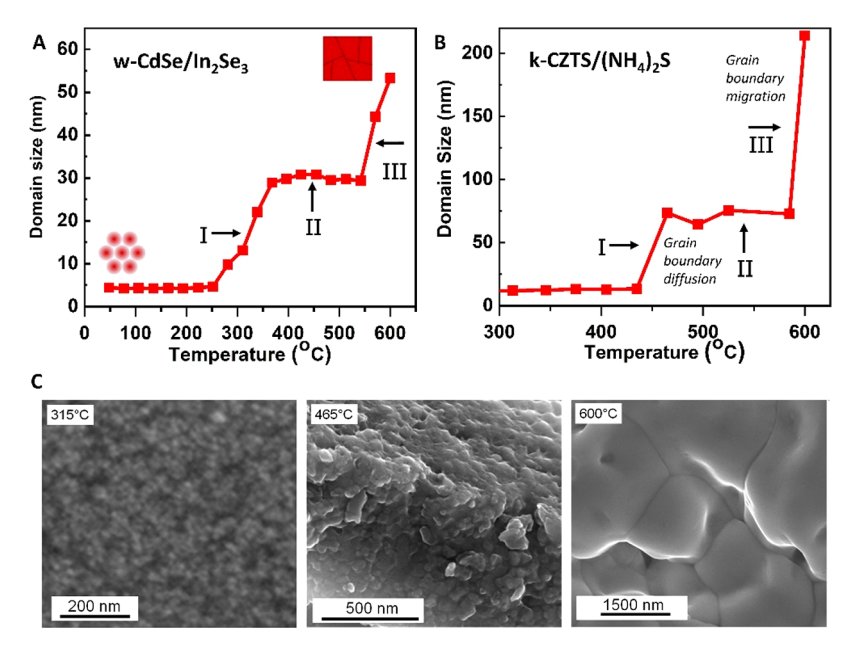


Figure 4. (A) Temperature-dependent grain growth profile of 4.2 nm w-CdSe NCs with  $(N_2H_5)_2In_2Se_4$  surface ligands. (B) Temperature-dependent grain growth profile for 12 nm kesterite CZTS NCs with  $(NH_4)_2S$  ligands. Both samples were characterized by monitoring X-ray diffraction upon continuous heating (in situ). (C) Cross-sectional SEM images of CZTS/ $(NH_4)_2S$  at 315 °C, 465 °C, and 600 °C corresponding to the three stages of sintering and grain growth as indicated in panel (B).

**3.7. Phenomenological Description of the Sintering Processes.** Sintering of crystalline particles has been extensively studied for ceramics and in powder metallurgy. The studies of ceramic powders revealed that sintering kinetics is often controlled by diffusion-limited mass transport such that the grain size (d) of ceramic powders scales as the square root of the annealing time  $(d \sim t^{1/2})$  at constant temperature, which is typical for diffusion-controlled processes. An exponent in t greater than 1/2 is usually considered as reflecting discontinuous grain growth, spurred by impurity doping or other factors. S6

The sintering kinetics is defined by the competition between several diffusion mechanisms shown in Scheme 1a, such as surface diffusion (defined by the diffusion coefficient  $D_{\text{surf}}$ ), diffusion along grain boundaries  $(D_{\rm gb})$ , and volume diffusion  $(D_{\text{vol}})$ . Atomic diffusion is a thermally activated process, and diffusion coefficients generally scale with temperature as D = $D_0 \exp(-E_A/k_BT)$ , where  $E_A$  is the activation energy for a particular diffusion mechanism;  $k_{\rm B}$  is the Boltzmann constant; and T is temperature. The surface atoms, due to their unsaturated bonding, have higher mobility and diffuse with lower activation energy compared to those of other diffusion channels. Similarly, undercoordinated lattice sites facilitate diffusion along grain boundaries (Scheme 1b), and grain boundary diffusion has a lower activation energy than volume diffusion. This hierarchy of energy scales determines the sequence of grain growth stages following gradual heating of a powdered material.

The sintering and grain growth processes can be qualitatively described in three stages, as demonstrated in Scheme 1c. <sup>50</sup> In the early stages, individual particles adhere to each other, forming necks. At low temperatures, surface diffusion is expected to be the dominant mass-transport mechanism responsible for the early stages of sintering and grain growth. The second stage, neck elongation, is observed at a higher temperature. It involves diffusion of atoms along grain boundaries between particles and causes the widening of necks

connecting adjacent crystalline domains. During the neck growth stage, grain boundaries do not move. At even higher temperatures, grain boundary migration enables the formation of large grains when the conditions are right, ultimately leading to a dense polycrystalline material that may contain macroscopic pores.

**3.8. Early Stage of Semiconductor NC Sintering and Grain Growth.** Scheme 1 was originally developed to describe sintering and grain growth of ceramic powders with rather large, micron size crystalline grains. NCs have much smaller, typically sub-10 nm crystalline domains and a correspondingly larger fraction of surface atoms. For example, the fraction of surface atoms in a 5 nm NC is above 20%. Naturally, this makes surface diffusion a key player during the early stage of NC sintering. The low activation energy for diffusion of atoms at NC surfaces has been demonstrated both experimentally and theoretically. S9-62

The differences in surface diffusion rates can explain the higher thermal stability of III-V NCs compared to II-VI NCs despite the significantly lower melting temperatures of the corresponding III-V phases. The chemical bonds in CdSe are more ionic than in InAs or InP, and the bond energies in III-V semiconductors (In-As: 201 kJ/mol) are significantly higher than those in II-VI (Cd-Se: 127.6 kJ/mol).<sup>63</sup> However, the absolute standard enthalpy of formation for bulk w-CdSe (H<sub>f</sub><sup>o</sup> = -159 kJ/mol) is more than twice as large as that for zb-InAs  $(H_f^0 = -60 \text{ kJ/mol})^{.64}$  These differences between local bond energies and enthalpies of formation for crystalline compounds confirm that the InAs bonds are mostly defined by covalent interactions between nearest neighbors, while in CdSe longrange electrostatic interactions make lattice energy less dependent on the local bonds. In a covalently bonded compound, surface diffusion requires breaking of short-ranged covalent bonds during atom movement, while in ionic crystals diffusing atoms interact with the collective electric field of multiple ions, forming the crystal lattice. Ionic bonding is therefore more delocalized and less sensitive to the nearestneighbor coordination environment and bond angles. As a result, the diffusion of  $Cd^{2+}$  and  $Se^{2-}$  ions on CdSe surfaces should be facilitated compared to the diffusion of In(III) and As(III) species on InAs NC surfaces. This is borne out by calculations from different literature sources: the energy barriers for Cd and Se diffusion on CdSe surfaces have been calculated to be between 0.2 and 0.4 eV, hile In diffusion on the InAs surface requires activation energies of 0.6–1 eV. For GaAs, the activation barrier for surface Ga diffusion has been measured and computed to be 1.3 eV.

The above arguments strongly suggest that sintering and grain growth onset temperatures in films of semiconductor NCs are related to the ionicity of NC atomic lattices. Ionic NCs are expected to sinter at lower temperatures compared to their covalently bound counterparts. The ionic character is further promoted in NCs with crystalline lattices with large coordination numbers, such as rock salt PbS and other lead chalcogenide NCs, which explains their low grain growth temperatures. High ionicity in crystalline lattices can also explain the low-temperature sintering and grain growth of CsPbX $_3$  (X = Cl, Br, I) NCs and other lead halide perovskite nanostructures.  $^{68,69}$ 

3.9. Late Stages of NC Sintering and Grain Growth. Surface diffusion results in material transfer toward necks and other regions with high local surface curvature (Scheme 1c). The driving force is the same as in Ostwald ripening—a system lowers its surface-to-volume ratio by eliminating the smallest grains and minimizing the number of dangling chemical bonds. We found that in many NC films the stage of early grain growth is followed by a plateau where an increase of the annealing temperature induces no further grain growth. Figure 4a shows the grain growth profile for 4.2 nm w-CdSe NCs, where three distinct regimes can be easily identified. The lowtemperature grain growth period ("I") is related to surface diffusion, which is followed by a temperature range ("II") where no appreciable grain growth takes place. Once the temperature is sufficiently high to overcome the activation barrier for grain boundary migration, there is again a stage of steep grain growth ("III"). This behavior was consistently observed for different NC sizes (Figure S10). Kesterite Cu<sub>2</sub>ZnSnS<sub>4</sub> (k-CZTS) NCs with ~12 nm size capped with (NH<sub>4</sub>)<sub>2</sub>S also showed a qualitatively similar grain growth profile (Figures 4b and S11), even though the grain growth started at higher temperatures and the final grain size was

The grain size evolution during the three stages of growth could be further tracked with electron microscopy. Figure 4c shows cross-sectional SEM images of (NH<sub>4</sub>)<sub>2</sub>S-capped k-CZTS NC films annealed at temperatures corresponding to sintering stages I, II, and III in Figure 4b. Randomly packed individual NCs can be seen after annealing at 313 °C. However, when the annealing temperature was increased to 465 °C, significantly larger, 50 to 80 nm, grains are observed in SEM, consistent with the Scherrer size calculated from P-XRD measurements. Finally, in the films annealed at 600 °C, the original ~12 nm k-CZTS NCs are transformed into a dense polycrystal with micron-size crystalline domains, which is again consistent with the sharp increase of the grain size at temperatures close to 600 °C in P-XRD measurements. Similar cross-sectional SEM measurements for w-CdSe NC films, corresponding to the P-XRD data in Figure 4a, are shown in Figure S12. TEM images provide additional insights into the microstructural development of NC films annealed to

different temperatures (Figure S13). In particular, substantial loss of porosity is seen at high temperatures, illustrated by the fusing together of the original NC grains into a nearly continuous film. The increase in density across the sample is consistent with the shrinkage of the substrate-deposited films that caused cracking in much thicker samples (Figure S2).

A survey of different NC materials capped with different inorganic ligands demonstrated the generality of grain growth stages I, II, and III for films of semiconductor NCs that do not undergo phase transitions, as discussed below. Depending upon the activation energies for surface diffusion and grain boundary migration in different compounds, stage II (no grain growth window) can span a wide or narrow temperature range. For example, in zb-CdTe NCs with  $(N_2H_5)_2In_2Te_4$  ligands, we were not able to observe stage III below 600 °C, the highest temperature used in this study (Figures S14 and S15). This could be explained by a high activation energy for grain boundary mobility in CdTe in the absence of grain growth promoters<sup>70</sup> and a relatively low sublimation temperature of CdTe. For III-V NCs, grain growth starts at high temperatures (Figure 2), and only stage I could be observed below our experimental ceiling of 600 °C. Heating to higher temperatures would not be useful, because both InP and InAs are prone to thermal decomposition above 600 °C.

The existence of stage II, stalled grain growth, is in most cases unfortunate because it prevents efficient conversion of NCs into polycrystalline solids under conditions compatible with most technologically important substrates. Typical grain sizes corresponding to the stage II plateau are too large to retain useful quantum-confined properties but too small for achieving carrier mobilites and diffusion lengths typical for solids with large crystalline domains. In some cases, proper surface engineering allows achieving excellent electronic properties in materials with sub-50 nm grains, 1 but such examples are not very common. Grain growth can be accelerated by the addition of grain growth promoters, such as CdCl<sub>2</sub> for CdTe,  $^{70}$  Mg<sup>2+</sup> for CeO<sub>2</sub>,  $^{72}$  or Sr<sup>2+</sup> for Y<sub>2</sub>O<sub>3</sub>. SF For semiconductors, this approach is not very useful because foreign impurities typically result in uncontrolled doping of the semiconducting phase. Only a few examples of grain growth promoters are known for technologically important II-VI semiconductors, and we are not aware of efficient promoters of grain growth in III-V semiconductors.

3.10. Acceleration of Grain Boundary Mobility during Phase Transitions. Solid-solid phase transitions are ubiquitous and important for many industrial and geological processes. An important case is the austenite to martensite phase transition, which is vital to improve steel hardness.<sup>73</sup> On the other hand, the retardation of tetragonal to monoclinic phase transition via addition of Y2O3 or MgO is required to make high-quality ZrO<sub>2</sub> ceramics.<sup>74</sup> Modern colloidal methods provide impressive versatility in the synthesis of various polymorphs corresponding to stable and metastable phases of different semiconductor NCs. Structural phase transitions are well-known in NCs and can be triggered by applying pressure or temperature. 75,776 Irreversible phase transitions of NCs from wurtzite to zinc blende or vice versa have been investigated both theoretically and experimentally. 60-62,77 For example, phase transition from a zb- to a w-ZnS phase has been explored in hydrothermal conditions and in solid samples at elevated temperatures. 60 The zinc blende phase is distinguished from wurtzite by different atom stacking sequences along the zinc blende (111) or wurtzite (001) crystal axes. It has been

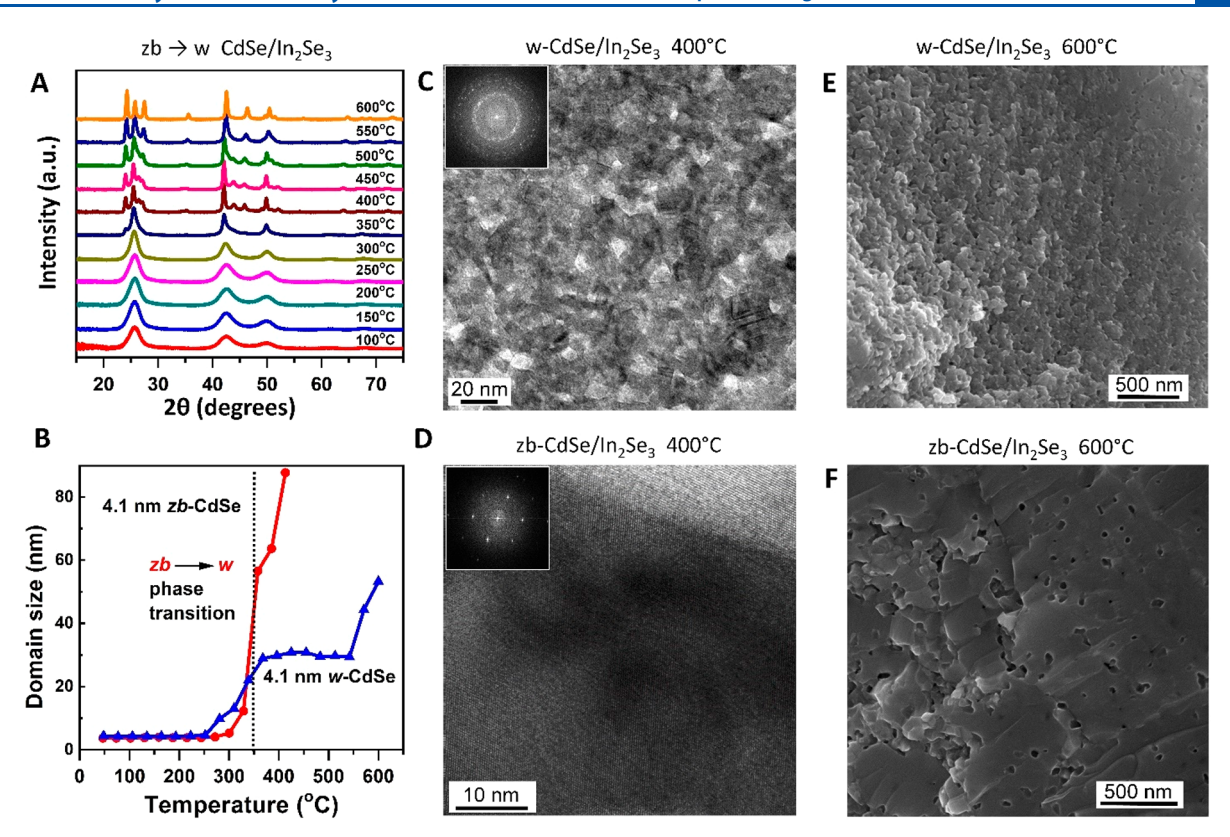


Figure 5. (A) X-ray diffraction patterns of zb-CdSe/In<sub>2</sub>Se<sub>4</sub><sup>2-</sup> films with increasing temperature. Notice the transformation from the zinc blende to wurtzite phase at 350 °C. (B) Temperature-dependent grain growth profiles of NC films with starting materials w-CdSe/In<sub>2</sub>Se<sub>4</sub><sup>2-</sup> and zb-CdSe/In<sub>2</sub>Se<sub>4</sub><sup>2-</sup>. The vertical line indicates the temperature where phase transition was observed. (C, D) TEM images of films annealed at 400 °C on TEM grids with starting materials: 4 nm w-CdSe/In<sub>2</sub>Se<sub>4</sub><sup>2-</sup> and zb-CdSe/In<sub>2</sub>Se<sub>4</sub><sup>2-</sup> NCs. The insets show fast-Fourier transforms of the entire image areas. (E, F) SEM images of films annealed at 600 °C with starting materials: 4 nm w-CdSe/In<sub>2</sub>Se<sub>4</sub><sup>2-</sup> and zb-CdSe/In<sub>2</sub>Se<sub>4</sub><sup>2-</sup> NCs.

proposed that switching between these two structures can be achieved by the defect-initiated simultaneous reorganization of strips of atoms. The phase boundary continuously moves through the NC until the new phase completely replaces the old one.  $^{79}$ 

It was previously observed that wurtzite-to-kesterite phase transition at elevated temperature led to enhanced grain growth in w-CZTS nanorods. 23,24,80 Here, we demonstrate the generality of this phenomenon for various nanomaterials synthesized as metastable polymorphs by colloidal methods. Figure 5a shows the change of P-XRD patterns of zb-CdSe NCs with (N<sub>2</sub>H<sub>5</sub>)<sub>2</sub>In<sub>2</sub>Se<sub>4</sub> ligands upon heating. The P-XRD peaks related to the thermodynamically stable w-CdSe phase first appear around ~350 °C and become much more pronounced at higher temperatures. There was some variation in the onset temperature of phase transition from sample to sample, probably related to minor differences in sample preparation, but in all samples this transition occurred between 300 and 400 °C. The zinc blende-to-wurtzite phase transition coincided with a steep increase in the grain size as shown in Figure 5b. Figure 5b also shows a direct comparison of grain size evolution with temperature for w-CdSe NCs of similar size capped with the same  $(N_2H_5)_2In_2Se_4$ . Such a comparison rules out the role of ligands as possible grain growth promoters in zb-CdSe NCs.

For CdSe NCs, grain growth was much faster when coupled to the phase transition, and the final grain size at a given temperature was much larger when we started with metastable zb-CdSe NCs. This was further confirmed by TEM and SEM analysis. TEM images showed necking and slight grain growth

at 350 °C for zb-CdSe NCs (Figure S16). Further heating to 400 °C resulted in a sudden increase in grain size. Large-area  $(\sim 0.1 \ \mu \text{m}^2)$  HRTEM images showed thin films with unperturbed atomic planes (Figure 5d). In contrast, w-CdSe NCs heated to the same annealing temperature showed large numbers of small crystalline domains tightly connected to each other (Figure 5c). This size evolution trend was corroborated by SEM images where grain size increased abruptly from 350 to 400 °C and then continued to grow, forming very large grains at 600 °C (cf., Figures 5e and 5f, S12, and S17). We observed very similar results for zb-CdSe NCs capped with (NH<sub>4</sub>)<sub>2</sub>S or "bare" NCs (Figures S18 and S19). These control experiments further rule out that impurity doping from ligands can be responsible for accelerated grain growth. In yet another control study, we tested the effect of substrate and compared the grain growth behavior of thin submicron films and thick pressed pellets of zb-CdSe NCs with (N<sub>2</sub>H<sub>5</sub>)<sub>2</sub>In<sub>2</sub>Se<sub>4</sub> ligands and observed no effect of film thickness on the grain growth behavior (Figure S20). Experiments with zb-CdSe NCs capped with bulky maleate ligands showed that no accelerated grain growth occurs if NC cores do not touch each other when the phase transition takes place (Figure S18).

Grain growth in CdSe NC films is related to the transition from the metastable cubic (zb) to hexagonal (w) phase, which raises a question about the possible role of crystal type in sintering and grain growth kinetics. For CdTe NCs, the stable and metastable phases are reversed, with thermodynamically stable zinc blende and metastable wurtzite. As in the case of CdSe, films of CdTe NCs with  $(N_2H_5)_2In_2Te_4$  ligands showed accelerated grain growth for metastable w-CdTe compared to

the zb-CdTe polymorph (Figure S15). Furthermore, essentially the same behavior was observed for the films of w-CZTS and k-CZTS NCs, where phase transition from the hexagonal (w) to cubic (k) phase resulted in accelerated grain growth (Figure S11). These examples demonstrate that both  $zb \rightarrow w$ and  $w \rightarrow zb$  phase transitions accelerate grain growth in NC films. The effect appears to be general, at least for chalcogenide semiconductor NCs. Surprisingly, little is known about the nature of this effect. The transformation of NCs from the metastable phase to the stable phase is an exothermic process which requires heating above the equilibrium phase transition temperature to overcome the nucleation barrier. We can estimate associated temperature change as  $\Delta T = \Delta E_{w-zb}/C_{v}$ where  $\Delta E_{w-zb}$  is the energy difference between wurtzite and zinc blende phases of a semiconductor material and  $C_p$  is the heat capacity. Both calculations and experimental data suggest that  $\Delta E_{\text{w-zb}}$  for II–VI semiconductors is below 10 meV/ atom, 81 while  $C_p$  for NCs is a weighted average of the bulk specific heat capacities of the inorganic core material and the ligands. For CdSe NCs, this quantity should be ~0.5 J g- $K^{-1.82}$  The resulting local temperature changes  $\Delta T$  associated with a phase transition should not exceed a few tens of Kelvin, which is not sufficient to explain a difference in grain size based on the temperature difference. Therefore, the effect of phase transitions on grain growth cannot be purely thermal. On the other hand, phase transition involves correlated rearrangement of atoms. The nucleation of a new phase is a low-probability event that occurs in a small number of NCs, leading to recrystallization fronts which propagate across multiple partially sintered NCs. Recent studies of solid-solid phase transitions also revealed transient formation of a liquid-like state separating two phases. 83,84 Formation of these disordered regions should dramatically increase ion mobility near the moving boundary, separating two phases during a solid-solid phase transition. A cascade of bond rearrangements during the phase transition can accelerate volume diffusion at temperatures where, in the absence of a phase transition, only surface diffusion would be possible. Both surface and volume diffusion processes contribute to align the crystal lattices of touching grains. Further experimental and theoretical studies will be necessary to fully understand the microscopic coupling between phase transitions and accelerated grain growth in NC films. We speculate that it can be a phenomenon inherent to nanoscale crystals, where the width of a transient disordered state during phase transition is comparable to NC size. For example, oriented attachment<sup>43</sup> and NC ion exchange reactions<sup>51</sup> are not common for bulk solids but are widely observed for NCs. From a practical point of view, accelerated grain growth can help make materials composed of large crystalline domains without applying very high temperatures or using grain growth promoters.

## 4. CONCLUSIONS

In summary, this systematic investigation of sintering and grain growth behavior in semiconductor NC solids has yielded several important insights. Our observations suggest that II—VI, IV—VI, and III—V semiconductor NCs have qualitatively different thermal stabilities and grain growth behaviors that can be traced to the peculiarities of ion diffusion in crystals with ionic or covalent bonding. Generally, covalently bonded III—V NCs have much better thermal stability than more ionic II—VI materials, while lead chalcogenide IV—VI NCs are the least thermally stable against recrystallization and grain growth.

Grain growth in NC films typically follows a pathway with two distinct kinetic regimes controlled by the surface diffusion at low temperatures and by grain boundary mobility at high temperatures. These regimes can be separated by a large temperature window with very slow grain growth. Phase transitions between wurtzite and zinc blende phases in chalcogenide NCs were found to greatly accelerate grain growth in NC films.

These observations can guide the rational selection of NC materials for fabricating thin-film optoelectronic devices using solution-processed NC inks. For devices utilizing quantum confinement effects in the visible spectral range, the thermal stability of InP NCs will be superior to that of CdSe NCs. For near-IR applications, films of InAs NCs will be far more thermally stable than films of PbS NCs. The latter material, and corresponding devices using PbS QDs, may not be able to tolerate heating above 100 °C for extended periods of time. NCs of metastable phases, such as zb-CdSe, may not be an optimal choice for high-temperature applications because solid-solid phase transitions greatly accelerate NC sintering and grain growth. On the other hand, metastable NCs could be excellent precursors for growing large crystallites at relatively low temperatures. NCs with small inorganic ligands are particularly useful for preparing NC films with large grains and may be utilized in preparing NC inks for large-area device fabrication.

#### ASSOCIATED CONTENT

# Supporting Information

The Supporting Information is available free of charge at https://pubs.acs.org/doi/10.1021/acs.jpcc.2c07400.

Additional experimental details, absorption spectra, SEM and TEM images, and powder X-ray diffraction patterns (PDF)

# AUTHOR INFORMATION

#### **Corresponding Author**

Dmitri V. Talapin — Department of Chemistry, James Franck Institute, and Pritzker School of Molecular Engineering, University of Chicago, Chicago, Illinois 60637, United States; Center for Nanoscale Materials, Argonne National Laboratory, Argonne, Illinois 60439, United States; orcid.org/0000-0002-6414-8587; Email: dvtalapin@uchicago.edu

#### Authors

Wenyong Liu — Department of Chemistry, James Franck Institute, and Pritzker School of Molecular Engineering, University of Chicago, Chicago, Illinois 60637, United States Vishwas Srivastava — Department of Chemistry, James Franck Institute, and Pritzker School of Molecular Engineering, University of Chicago, Chicago, Illinois 60637, United States

J. Matthew Kurley — Department of Chemistry, James Franck Institute, and Pritzker School of Molecular Engineering, University of Chicago, Chicago, Illinois 60637, United States; © orcid.org/0000-0003-0592-0714

Chengyang Jiang — Department of Chemistry, James Franck Institute, and Pritzker School of Molecular Engineering, University of Chicago, Chicago, Illinois 60637, United States

Complete contact information is available at: https://pubs.acs.org/10.1021/acs.jpcc.2c07400

#### Notes

The authors declare no competing financial interest.

### ACKNOWLEDGMENTS

We thank Andrew Nelson for editing the manuscript. This work on the synthesis and functionalization of nanomaterials was supported by the Center for Hierarchical Materials Design (CHiMad) supported by the U.S. Department of Commerce, National Institute of Standards and Technology, under financial assistance award number 70NANB14H012. The sintering and grain growth kinetics studies were supported by the National Science Foundation under award number DMR-2004880. V.S. was supported by the University of Chicago Materials Research Science and Engineering Center, which is funded by the National Science Foundation under award number DMR-2011854. This research used resources of the Center for Nanoscale Materials, a U.S. Department of Energy (DOE) Office of Science User Facility operated for the DOE Office of Science by Argonne National Laboratory under Contract No. DE-AC02-06CH11357.

#### REFERENCES

- (1) Murray, C. B.; Norris, D. J.; Bawendi, M. G. Synthesis and Characterization of Nearly Monodisperse CdE (E = Sulfur, Selenium, Tellurium) Semiconductor Nanocrystallites. *J. Am. Chem. Soc.* **1993**, *115* (19), 8706–8715.
- (2) Borys, N. J.; Walter, M. J.; Huang, J.; Talapin, D. V.; Lupton, J. M. The Role of Particle Morphology in Interfacial Energy Transfer in CdSe/CdS Heterostructure Nanocrystals. *Science* **2010**, 330 (6009), 1371–1374
- (3) Yu, D.; Wang, C.; Guyot-Sionnest, P. N-Type Conducting CdSe Nanocrystal Solids. *Science* **2003**, *300* (5623), 1277–1280.
- (4) Talapin, D. V.; Murray, C. B. PbSe Nanocrystal Solids for N-and P-Channel Thin Film Field-Effect Transistors. *Science* **2005**, *310* (5745), 86–89.
- (5) McDonald, S. A.; Konstantatos, G.; Zhang, S.; Cyr, P. W.; Klem, E. J. D.; Levina, L.; Sargent, E. H. Solution-Processed PbS Quantum Dot Infrared Photodetectors and Photovoltaics. *Nat. Mater.* **2005**, *4* (2), 138–142.
- (6) Lee, J.-S.; Kovalenko, M. V.; Huang, J.; Chung, D. S.; Talapin, D. V. Band-Like Transport, High Electron Mobility and High Photoconductivity in All-Inorganic Nanocrystal Arrays. *Nat. Nanotechnol.* **2011**, *6* (6), 348–352.
- (7) Liu, W.; Lee, J.-S.; Talapin, D. V. III-V Nanocrystals Capped with Molecular Metal Chalcogenide Ligands: High Electron Mobility and Ambipolar Photoresponse. *J. Am. Chem. Soc.* **2013**, *135* (4), 1349–1357.
- (8) Tang, J.; Kemp, K. W.; Hoogland, S.; Jeong, K. S.; Liu, H.; Levina, L.; Furukawa, M.; Wang, X.; Debnath, R.; Cha, D.; et al. Colloidal-Quantum-Dot Photovoltaics Using Atomic-Ligand Passivation. *Nat. Mater.* **2011**, *10* (10), 765–771.
- (9) Jasieniak, J.; MacDonald, B. I.; Watkins, S. E.; Mulvaney, P. Solution-Processed Sintered Nanocrystal Solar Cells Via Layer-by-Layer Assembly. *Nano Lett.* **2011**, *11* (7), 2856–2864.
- (10) Panthani, M. G.; Kurley, J. M.; Crisp, R. W.; Dietz, T. C.; Ezzyat, T.; Luther, J. M.; Talapin, D. V. High Efficiency Solution Processed Sintered CdTe Nanocrystal Solar Cells: The Role of Interfaces. *Nano Lett.* **2014**, *14* (2), 670–675.
- (11) Guo, Q.; Ford, G. M.; Yang, W.-C.; Walker, B. C.; Stach, E. A.; Hillhouse, H. W.; Agrawal, R. Fabrication of 7.2% Efficient CZTSSe Solar Cells Using CZTS Nanocrystals. *J. Am. Chem. Soc.* **2010**, *132* (49), 17384–17386.
- (12) Barsoum, M. W. Fundamentals of Ceramics; Routledge: New York, 2002.
- (13) Ihly, R.; Tolentino, J.; Liu, Y.; Gibbs, M.; Law, M. The Photothermal Stability of PbS Quantum Dot Solids. *ACS Nano* **2011**, 5 (10), 8175–8186.

- (14) Goodfellow, B. W.; Patel, R. N.; Panthani, M. G.; Smilgies, D.-M.; Korgel, B. A. Melting and Sintering of a Body-Centered Cubic Superlattice of PbSe Nanocrystals Followed by Small Angle X-Ray Scattering. *J. Phys. Chem. C* **2011**, *115* (14), 6397–6404.
- (15) German, R. M. Sintering Theory and Practice; Wiley-VCH: Weinheim, Germany, 1996.
- (16) Rahaman, M. N. Sintering of Ceramics; CRC Press: Boca Raton, 2008.
- (17) Rahaman, M. N. Ceramic Processing; CRC Press: Boca Raton, 2006.
- (18) Lu, J.; Fu, B.; Kung, M. C.; Xiao, G.; Elam, J. W.; Kung, H. H.; Stair, P. C. Coking- and Sintering-Resistant Palladium Catalysts Achieved through Atomic Layer Deposition. *Science* **2012**, 335 (6073), 1205–1208.
- (19) Choi, M.; Wu, Z.; Iglesia, E. Mercaptosilane-Assisted Synthesis of Metal Clusters within Zeolites and Catalytic Consequences of Encapsulation. *J. Am. Chem. Soc.* **2010**, 132 (26), 9129–9137.
- (20) Hermes, S.; Schröter, M.-K.; Schmid, R.; Khodeir, L.; Muhler, M.; Tissler, A.; Fischer, R. W.; Fischer, R. A. Metal@MOF: Loading of Highly Porous Coordination Polymers Host Lattices by Metal Organic Chemical Vapor Deposition. *Angew. Chem., Int. Ed.* **2005**, 44 (38), 6237–6241.
- (21) Lee, J.; Farha, O. K.; Roberts, J.; Scheidt, K. A.; Nguyen, S. T.; Hupp, J. T. Metal-Organic Framework Materials as Catalysts. *Chem. Soc. Rev.* **2009**, *38* (5), 1450–1459.
- (22) Zhang, W.; Lu, G.; Cui, C.; Liu, Y.; Li, S.; Yan, W.; Xing, C.; Chi, Y. R.; Yang, Y.; Huo, F. A Family of Metal-Organic Frameworks Exhibiting Size-Selective Catalysis with Encapsulated Noble-Metal Nanoparticles. *Adv. Mater.* **2014**, *26* (24), 4056–4060.
- (23) Mainz, R.; Singh, A.; Levcenko, S.; Klaus, M.; Genzel, C.; Ryan, K. M.; Unold, T. Phase-Transition-Driven Growth of Compound Semiconductor Crystals from Ordered Metastable Nanorods. *Nat. Commun.* **2014**, DOI: 10.1038/ncomms4133.
- (24) Singh, A.; Lutz, L.; Ong, G. K.; Bustillo, K.; Raoux, S.; Jordan-Sweet, J. L.; Milliron, D. J. Controlling Morphology in Polycrystalline Films by Nucleation and Growth from Metastable Nanocrystals. *Nano Lett.* **2018**, *18* (9), 5530–5537.
- (25) Jiang, C.; Lee, J.-S.; Talapin, D. V. Soluble Precursors for CuInSe<sub>2</sub>, CuIn<sub>1-x</sub>Ga<sub>x</sub>Se<sub>2</sub>, and Cu<sub>2</sub>ZnSn(S,Se)<sub>4</sub> Based on Colloidal Nanocrystals and Molecular Metal Chalcogenide Surface Ligands. *J. Am. Chem. Soc.* **2012**, *134* (11), 5010–5013.
- (26) Kovalenko, M. V.; Scheele, M.; Talapin, D. V. Colloidal Nanocrystals with Molecular Metal Chalcogenide Surface Ligands. *Science* **2009**, 324 (5933), 1417–1420.
- (27) Choi, J.-H.; Fafarman, A. T.; Oh, S. J.; Ko, D.-K.; Kim, D. K.; Diroll, B. T.; Muramoto, S.; Gillen, J. G.; Murray, C. B.; Kagan, C. R. Bandlike Transport in Strongly Coupled and Doped Quantum Dot Solids: A Route to High-Performance Thin-Film Electronics. *Nano Lett.* 2012, 12 (5), 2631–2638.
- (28) Jang, J.; Liu, W.; Son, J. S.; Talapin, D. V. Temperature-Dependent Hall and Field-Effect Mobility in Strongly Coupled All-Inorganic Nanocrystal Arrays. *Nano Lett.* **2014**, *14* (2), 653–662.
- (29) Mitzi, D. B.; Kosbar, L. L.; Murray, C. E.; Copel, M.; Afzali, A. High-Mobility Ultrathin Semiconducting Films Prepared by Spin Coating. *Nature* **2004**, 428 (6980), 299–303.
- (30) Mitzi, D. B.  $N_4H_9Cu_7S_4$ : A Hydrazinium-Based Salt with a Layered  $Cu_7S_4$ <sup>-</sup> Framework. *Inorg. Chem.* **2007**, *46* (3), 926–931.
- (31) Wilson, D.; Langell, M. XPS Analysis of Oleylamine/Oleic Acid Capped Fe<sub>3</sub>O<sub>4</sub> Nanoparticles as a Function of Temperature. *Appl. Surf. Sci.* **2014**, 303, 6–13.
- (32) Chen, O.; Chen, X.; Yang, Y.; Lynch, J.; Wu, H.; Zhuang, J.; Cao, Y. C. Synthesis of Metal-Selenide Nanocrystals Using Selenium Dioxide as the Selenium Precursor. *Angew. Chem., Int. Ed.* **2008**, 47 (45), 8638–8641.
- (33) Carbone, L.; Nobile, C.; De Giorgi, M.; Sala, F. D.; Morello, G.; Pompa, P.; Hytch, M.; Snoeck, E.; Fiore, A.; Franchini, I. R.; et al. Synthesis and Micrometer-Scale Assembly of Colloidal CdSe/CdS Nanorods Prepared by a Seeded Growth Approach. *Nano Lett.* **2007**, 7 (10), 2942–2950.

- (34) Yu, W. W.; Wang, Y. A.; Peng, X. Formation and Stability of Size-, Shape-, and Structure-Controlled CdTe Nanocrystals: Ligand Effects on Monomers and Nanocrystals. *Chem. Mater.* **2003**, *15* (22), 4300–4308.
- (35) Micic, O. I.; Curtis, C. J.; Jones, K. M.; Sprague, J. R.; Nozik, A. J. Synthesis and Characterization of InP Quantum Dots. *J. Phys. Chem.* **1994**, *98* (19), 4966–4969.
- (36) Guzelian, A. A.; Banin, U.; Kadavanich, A. V.; Peng, X.; Alivisatos, A. P. Colloidal Chemical Synthesis and Characterization of InAs Nanocrystal Quantum Dots. *Appl. Phys. Lett.* **1996**, *69* (10), 1432–1434.
- (37) Hines, M. A.; Scholes, G. D. Colloidal PbS Nanocrystals with Size-Tunable near-Infrared Emission: Observation of Post-Synthesis Self-Narrowing of the Particle Size Distribution. *Adv. Mater.* **2003**, *15* (21), 1844–1849.
- (38) Riha, S. C.; Parkinson, B. A.; Prieto, A. L. Solution-Based Synthesis and Characterization of Cu<sub>2</sub>ZnSnS<sub>4</sub> Nanocrystals. *J. Am. Chem. Soc.* **2009**, *131* (34), 12054–12055.
- (39) Jao, M.-H.; Liao, H.-C.; Wu, M.-C.; Su, W.-F. Synthesis and Characterization of Wurtzite Cu<sub>2</sub>ZnSnS<sub>4</sub> Nanocrystals. *Jpn. J. Appl. Phys.* **2012**, *51* (10S), 10NC30.
- (40) Zhang, H.; Hu, B.; Sun, L.; Hovden, R.; Wise, F. W.; Muller, D. A.; Robinson, R. D. Surfactant Ligand Removal and Rational Fabrication of Inorganically Connected Quantum Dots. *Nano Lett.* **2011**, *11* (12), 5356–5361.
- (41) Nag, A.; Kovalenko, M. V.; Lee, J.-S.; Liu, W.; Spokoyny, B.; Talapin, D. V. Metal-Free Inorganic Ligands for Colloidal Nanocrystals: S<sup>2-</sup>, HS<sup>-</sup>, Se<sup>2-</sup>, HSe<sup>-</sup>, Te<sup>2-</sup>, HTe<sup>-</sup>, TeS<sub>3</sub><sup>2-</sup>, OH<sup>-</sup>, and NH<sub>2</sub><sup>-</sup> as Surface Ligands. *J. Am. Chem. Soc.* **2011**, *133* (27), 10612–10620.
- (42) Rosen, E. L.; Buonsanti, R.; Llordes, A.; Sawvel, A. M.; Milliron, D. J.; Helms, B. A. Exceptionally Mild Reactive Stripping of Native Ligands from Nanocrystal Surfaces by Using Meerwein's Salt. *Angew. Chem., Int. Ed.* **2012**, *51* (3), 684–689.
- (43) Cho, K.-S.; Talapin, D. V.; Gaschler, W.; Murray, C. B. Designing PbSe Nanowires and Nanorings through Oriented Attachment of Nanoparticles. *J. Am. Chem. Soc.* **2005**, *127* (19), 7140–7147.
- (44) Scott, G.; Kilgour, D. The Density of Random Close Packing of Spheres. J. Phys. D: Appl. Phys. 1969, 2 (6), 863.
- (45) Bernal, J. D.; Mason, J. Packing of Spheres: Co-ordination of Randomly Packed Spheres. *Nature* **1960**, *188* (4754), 910–911.
- (46) Takagi, M. Electron-Diffraction Study of Liquid-Solid Transition of Thin Metal Films. *J. Phys. Chem. Soc. Jpn.* **1954**, 9 (3), 359–363.
- (47) Goldstein, A. N.; Echer, C. M.; Alivisatos, A. P. Melting in Semiconductor Nanocrystals. *Science* **1992**, 256 (5062), 1425–1427.
- (48) Mitzi, D. B.; Copel, M.; Chey, S. J. Low-Voltage Transistor Employing a High-Mobility Spin-Coated Chalcogenide Semiconductor. *Adv. Mater.* **2005**, *17* (10), 1285–1289.
- (49) Bordia, R. K.; Jagota, A. Crack Growth and Damage in Constrained Sintering Films. *J. Am. Ceram. Soc.* **1993**, 76 (10), 2475–2485
- (50) Kang, S.-J. L. Sintering: Densification, Grain Growth and Microstructure; Elsevier, 2004.
- (51) Son, D. H.; Hughes, S. M.; Yin, Y.; Paul Alivisatos, A. Cation Exchange Reactions in Ionic Nanocrystals. *Science* **2004**, *306* (5698), 1009–1012.
- (52) Woodward, J. T.; Ulman, A.; Schwartz, D. K. Self-Assembled Monolayer Growth of Octadecylphosphonic Acid on Mica. *Langmuir* **1996**, 12 (15), 3626–3629.
- (53) Jiao, Y.; Han, D.; Liu, L.; Ji, L.; Guo, G.; Hu, J.; Yang, D.; Dong, A. Highly Ordered Mesoporous Few-Layer Graphene Frameworks Enabled by Fe<sub>3</sub>O<sub>4</sub> Nanocrystal Superlattices. *Angew. Chem., Int. Ed.* **2015**, *54* (19), 5727–5731.
- (54) Landman, U.; Luedtke, W. D. Small Is Different: Energetic, Structural, Thermal, and Mechanical Properties of Passivated Nanocluster Assemblies. *Faraday Discuss.* **2004**, *125* (0), 1–22.

- (55) Chen, P. L.; Chen, I. W. Grain Boundary Mobility in  $Y_2O_3$ : Defect Mechanism and Dopant Effects. *J. Am. Ceram. Soc.* **1996**, 79 (7), 1801–1809.
- (56) Coble, R. L. Sintering Crystalline Solids. I. Intermediate and Final State Diffusion Models. J. Appl. Phys. 1961, 32 (5), 787–792.
- (57) Invenson, V. Densification of Metal Powders During Sintering; Plenum: New York, 1973.
- (58) Smith, A. M.; Nie, S. Semiconductor Nanocrystals: Structure, Properties, and Band Gap Engineering. *Acc. Chem. Res.* **2010**, 43 (2), 190–200.
- (59) Buesser, B.; Grohn, A.; Pratsinis, S. E. Sintering Rate and Mechanism of TiO<sub>2</sub> Nanoparticles by Molecular Dynamics. *J. Phys. Chem. C* **2011**, *115* (22), 11030–11035.
- (60) Zhang, H.; Huang, F.; Gilbert, B.; Banfield, J. F. Molecular Dynamics Simulations, Thermodynamic Analysis, and Experimental Study of Phase Stability of Zinc Sulfide Nanoparticles. *J. Phys. Chem. B* **2003**, *107* (47), 13051–13060.
- (61) Zhang, H.; Gilbert, B.; Huang, F.; Banfield, J. F. Water-Driven Structure Transformation in Nanoparticles at Room Temperature. *Nature* **2003**, 424 (6952), 1025.
- (62) Zhang, H.; Banfield, J. F. Aggregation, Coarsening, and Phase Transformation in ZnS Nanoparticles Studied by Molecular Dynamics Simulations. *Nano Lett.* **2004**, *4* (4), 713–718.
- (63) Luo, Y.-R. Comprehensive Handbook of Chemical Bond Energies; CRC Press: Boca Raton, 2007.
- (64) CRC Handbook of Chemistry and Physics, 92nd ed.; CRC Press: Boca Raton, 2012.
- (65) Rempel, J. Y.; Trout, B. L.; Bawendi, M. G.; Jensen, K. F. Properties of the CdSe(0001), (0001), and (1120) Single Crystal Surfaces: Relaxation, Reconstruction, and Adatom and Admolecule Adsorption. *J. Phys. Chem. B* 2005, 109 (41), 19320–19328.
- (66) Stevens, M. A.; Tomasulo, S.; Maximenko, S.; Vandervelde, T. E.; Yakes, M. K. Surface Diffusion Measurements of In on InGaAs Enabled by Droplet Epitaxy. *J. Appl. Phys.* **2017**, *121* (19), 195302.
- (67) Bietti, S.; Somaschini, C.; Esposito, L.; Fedorov, A.; Sanguinetti, S. Gallium Surface Diffusion on GaAs (001) Surfaces Measured by Crystallization Dynamics of Ga Droplets. *J. Appl. Phys.* **2014**, *116* (11), 114311.
- (68) Yuan, X.; Hou, X.; Li, J.; Qu, C.; Zhang, W.; Zhao, J.; Li, H. Thermal Degradation of Luminescence in Inorganic Perovskite CsPbBr<sub>3</sub> Nanocrystals. *Phys. Chem. Chem. Phys.* **2017**, *19* (13), 8934–8940.
- (69) Diroll, B. T.; Nedelcu, G.; Kovalenko, M. V.; Schaller, R. D. High-Temperature Photoluminescence of CsPbX<sub>3</sub> (X = Cl, Br, I) Nanocrystals. *Adv. Funct. Mater.* **2017**, 27 (21), 1606750.
- (70) Zhang, H.; Kurley, J. M.; Russell, J. C.; Jang, J.; Talapin, D. V. Solution-Processed, Ultrathin Solar Cells from CdCl<sub>3</sub><sup>-</sup>-Capped CdTe Nanocrystals: The Multiple Roles of CdCl<sub>3</sub><sup>-</sup> Ligands. *J. Am. Chem. Soc.* **2016**, *138* (24), 7464–7467.
- (71) Dolzhnikov, D. S.; Zhang, H.; Jang, J.; Son, J. S.; Panthani, M. G.; Shibata, T.; Chattopadhyay, S.; Talapin, D. V. Composition-Matched Molecular "Solders" for Semiconductors. *Science* **2015**, 347 (6220), 425.
- (72) Chen, P.-L.; Chen, I. W. Grain Growth in CeO<sub>2</sub>: Dopant Effects, Defect Mechanism, and Solute Drag. *J. Am. Ceram. Soc.* **1996**, 79 (7), 1793–1800.
- (73) Stringfellow, R.; Parks, D.; Olson, G. A Constitutive Model for Transformation Plasticity Accompanying Strain-Induced Martensitic Transformations in Metastable Austenitic Steels. *Acta Metall. Mater.* **1992**, *40* (7), 1703–1716.
- (74) Hannink, R. H.; Kelly, P. M.; Muddle, B. C. Transformation Toughening in Zirconia-Containing Ceramics. *J. Am. Ceram. Soc.* **2000**, 83 (3), 461–487.
- (75) Tolbert, S. H.; Alivisatos, A. The Wurtzite to Rock Salt Structural Transformation in CdSe Nanocrystals under High Pressure. *J. Chem. Phys.* **1995**, *102* (11), 4642–4656.
- (76) Zheng, H.; Rivest, J. B.; Miller, T. A.; Sadtler, B.; Lindenberg, A.; Toney, M. F.; Wang, L.-W.; Kisielowski, C.; Alivisatos, A. P.

Observation of Transient Structural-Transformation Dynamics in a Cu<sub>2</sub>S Nanorod. *Science* **2011**, 333 (6039), 206–209.

- (77) Jacobs, K.; Zaziski, D.; Scher, E. C.; Herhold, A. B.; Alivisatos, A. P. Activation Volumes for Solid-Solid Transformations in Nanocrystals. *Science* **2001**, 293 (5536), 1803–1806.
- (78) Glas, F. A Simple Calculation of Energy Changes Upon Stacking Fault Formation or Local Crystalline Phase Transition in Semiconductors. *J. Appl. Phys.* **2008**, *104* (9), 093520.
- (79) Banerjee, R; Jayakrishnan, R; Banerjee, R; Ayyub, P Effect of the Size-Induced Structural Transformation on the Band Gap in CdS Nanoparticles. *J. Phys: Cond. Mater.* **2000**, *12* (50), 10647.
- (80) Jiang, C.; Liu, W.; Talapin, D. V. Role of Precursor Reactivity in Crystallization of Solution-Processed Semiconductors: The Case of Cu<sub>2</sub>ZnSnS<sub>4</sub>. *Chem. Mater.* **2014**, *26* (13), 4038–4043.
- (81) Yeh, C.-Y.; Lu, Z. W.; Froyen, S.; Zunger, A. Zinc-Blende-Wurtzite Polytypism in Semiconductors. *Phys. Rev. B* **1992**, 46 (16), 10086–10097.
- (82) Ong, W.-L.; Rupich, S. M.; Talapin, D. V.; McGaughey, A. J. H.; Malen, J. A. Surface Chemistry Mediates Thermal Transport in Three-Dimensional Nanocrystal Arrays. *Nat. Mater.* **2013**, *12* (5), 410–415.
- (83) Pogatscher, S.; Leutenegger, D.; Schawe, J. E. K.; Uggowitzer, P. J.; Löffler, J. F. Solid-Solid Phase Transitions Via Melting in Metals. *Nat. Commun.* **2016**, *7* (1), 11113.
- (84) Peng, Y.; Wang, F.; Wang, Z.; Alsayed, A. M.; Zhang, Z.; Yodh, A. G.; Han, Y. Two-Step Nucleation Mechanism in Solid-Solid Phase Transitions. *Nat. Mater.* **2015**, *14* (1), 101–108.

# ☐ Recommended by ACS

# **Dual Atomic Coherence in the Self-Assembly of Patchy Heterostructural Nanocrystals**

Hua Zhu, Ou Chen, et al.

SEPTEMBER 01, 2022

ACS NANO

READ 🗹

# Asymmetric Interfacet Adatom Migration as a Mode of Anisotropic Nanocrystal Growth

Paul Z. Chen, Frank X. Gu, et al.

OCTOBER 13, 2022

JOURNAL OF THE AMERICAN CHEMICAL SOCIETY

READ 🗹

# **Exploring Nanoscale Structure in Perovskite Precursor Solutions Using Neutron and Light Scattering**

Mary E. O'Kane, Andrew J. Parnell, et al.

AUGUST 03, 2022

CHEMISTRY OF MATERIALS

READ

# Observation of an Orientational Glass in a Superlattice of Elliptically-Faceted CdSe Nanocrystals

Abdullah S. Abbas, A. Paul Alivisatos, et al.

MAY 24, 2022

ACS NANO

READ 🗹

Get More Suggestions >